Effective Parameters on Cladded Plate Delamination During Pressure Vessels Head Manufacturing by FEM and DOE

Mahmoud Afshari [a]*, Alireza Fallahi Arezodar [a], Iraj Sattarifar [a], Amirhossein Alavi [b]

[a] Department of Mechanical Engineering, Amirkabir University of Technology, Tehran, Iran..
[b] Department of Mechanical Engineering, University of Birjand, Birjand, Iran..
*corresponding author: Mahmoud Afshari, Email: m.afshari@aut.ac.ir

Article History: Received: 14 July 2020; Accepted: 2 January 2021; Published online: 5 February 2021

Abstract: Roll-bond cladded plates Have found extensive industrial applications. Stainless steels, Ni, Cu, and Ti have been usually employed as clad. In multi-piece head manufacturing, delamination may occur during pressing these plates into petals. In this paper, the effective parameters on delamination were investigated. SA 516 GR 70 and SS 316L were respectively selected as the base plate and clad due to their higher applications. First, the strain energy release rate (SERR) was assessed as the main criterion for the definition of delamination and the explanatory parameter using the finite element technique and virtual crack closure technique (VCCT) method. The interface was modeled as a cohesive zone with the tied mesh technique and validated by the experimental results. The response surface methodology (RSM) was employed as a design of experiment method to evaluate the effect of input parameters on the outputs (SERR). The results indicated the greater influence of the head radius on G followed by the thickness of the plate, pressing force, the number of pressing steps, shear strength, and friction coefficient. By enhancing the radius of the head and shear strength, SERR was decreased. The impact of the head radius was much greater than that of shear strength. Finally, some strategies have been proposed to prevent delamination.

Keywords: Roll-Bond clad plate, Delamination, VCCT, Tied Mesh method, FEM, SERR, DOE.

1. Introduction

Cladded plates have been widely used in the manufacturing of pressure vessels (PV) and pipes. Ferrite and austenitic stainless steels, nickel-based alloys, copper and its alloys, and titanium are among the materials used as the clad. The cladded layer may be separated from the base metal giving rise to delamination in the case of using Roll-bond-cladded plates when forming the PV head through pressing due to the low strength of the joint interface. Therefore, the behavior of such materials should be investigated under mechanical loading to prevent delamination.

The mechanical behavior of multilayer metals has been extensively discussed in various articles and diverse solutions have been proposed to improve their mechanical properties including flexural and fracture toughness and fatigue features.

Lee and et al. [1] reported that the tensile strength of the multilayer sheets can be predicted by the rule of averages. However, the formability of these sheets is usually less than the amount prescribed by this rule. Some researchers [2], [3], [4] assumed these plates as the metallic layer composites and used some equations governing their failure. This assumption was also used in this article. Tschegg et al. [5] conducted a three-point bending test on a specimen with cracks in the intermediate area and showed that both J integral and crack tip openings displacement (CTOD) steadily decreased as the crack distance approached the intermediate region. They also showed that the substrate cracks and even the interlayer cracks had inherent asymmetry and the cracks within the softer layer do not tend to approach the intermediate zone. According to their results, the force required to extend the interlayer crack is about half the force required to propagate the crack in each layer. Carreno et al. [2] examined the fracture behavior of these sheets and concluded that the crack growth in the bonding layer is not a function of the crack movement in the adjacent layer and follows its own terms and conditions.

Sung et. al [6] performed tensile and bending tests on roll-bond cladded plates in two heat-treated and as-rolled modes. They showed that annealing increased the ductility of the bond. Liu et. al [7] summarized and analyzed the effects of manufacturing process parameters on interface shear strength of stainless steel clad plate, including surface preparation, rolling reduction ratio, vacuum degree, rolling temperature and the number of rolling passes, as well as bonding interface microstructure, interface alloy element diffusion, heat treatment behavior and bonding mechanisms are

In this paper, the effect of forming process parameters (pressing force, number of loading steps, head radius, plate thickness, friction coefficient, and shear peeling strength) on the delamination in the cladded plates was investigated by the design of experiment and finite element methods. The strain rate release rate criterion was considered as the separation criterion and the effect of the process parameters was assessed using a validated finite element model. Finally, the mathematical relationship between these parameters and the separation criterion was addressed and the effect of each of these parameters was discussed in detail.

Delamination Criteria

Different criteria have been adopted to examine crack growth in the objects. In this paper, the strain energy release rate (SERR or G) criterion was used. The most important features of this criterion compared are its ability to explain the brittle behavior of the bonding region, relatively simple analytic relationships, and applicability to anisotropic materials [8] and layered composite problems [9] [10] [11], as well as the ability to evaluate its critical value through testing on non-standard specimens (in terms of the force-displacement curve area) [8].

The parameter of SERR was first proposed by Griffith [12] to explain the crack growth in a completely brittle sample. According to his analysis, SERR can be defined as the potential energy change, Π, in a cracked linear elastic system. The nucleation and crack growth occur when this energy reaches its critical limit, G_C. In this paper, the type of loading was assumed as mode II, considering the physics of the problem. Therefore, the relationships based on this mode was used for the end notched flexure (ENF) specimen (Figure 1). This sample, first proposed by Russell and Street [13], has a simple geometry, clamping, and computation. G_{II} values can be obtained based on the initial crack length and beam theory regardless of shear stress:

$$G_{\mathrm{II}} = \frac{9P^2a^2}{16b^2h^3E_{11}} \qquad (1)$$

$$G_{\mathrm{II}} = \frac{9a^2P\Delta}{2b(3a^3+2L^3)} \qquad (2)$$

In the above equations, P is the force value at the breakpoint, Δ shows the mid-point deflection of the beam, b represents the sample width, h denotes half of the beam thickness and l is the half-distance of the two supports. These equations were applied to standard specimens with equal thicknesses and the bonding region properties. Ouyang and Li [14] generalized Equation 2 for the cases with different two-layer thickness and properties. They found that failure mode II under pure shear loading had very little dependence on crack length. They also showed that shear bond strength is the most important parameter in determining the critical load. For similar shear strengths, the critical load does not increase with increasing Mode II toughness. According to their analysis, the strain release rate in Mode II can be determined by the following equation:

$$G_{\mathrm{II}}(J/m^2) = \frac{\frac{1}{2}\left[\frac{h_1 a}{2D_1}Q_T\right]^2 + \frac{(h_1+h_2)Q_T}{2(D_1+D_2)}\delta_0}{\frac{1}{A_1}+\frac{1}{A_2}+\frac{(h_1+h_2)^2}{4(D_1+D_2)}} \qquad (3)$$

Where

$$D_i = \frac{E_{xi}h_i^3}{12(1-\nu_{xzi}\nu_{zxi})}$$

And

$$A_i = \frac{E_{xi}h_i}{1-\nu_{xzi}\nu_{zxi}}$$

Index i = 1,2 represents beams 1 and 2 while A_i and D_i are axial and flexural stiffness units of beam width, respectively, under plane strain conditions. Q_T and h are the reaction force of the substrate and the thickness of the layers, respectively. In this paper, Equation 3 was applied to determine G_{IIC} having the critical force (Fcr)obtained by the three-point bending test and the critical relative slip value, δcr.

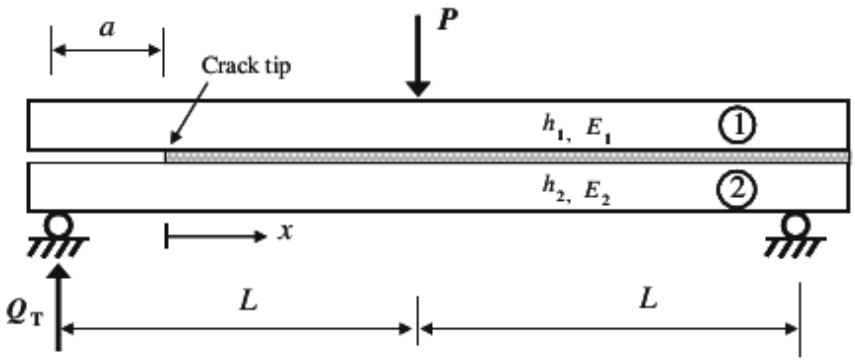

Figure 1: ENF Specimen.

Experimental procedure

To validate the finite element model (FEM), a three-point bending test was performed on the roll-bonded clad plate specimen. The sample length and width were 150 and 30 mm, respectively; while the thickness of the clad layer and the base metal were respectively set at 3mm and 22 mm. The crack length was 15 mm (Fig. 2). The mechanical properties of the plate are listed in Tables 1 and 2 based on the certificate issued by the manufacturer. The shear strength of the layers was determined as 382 MPa through a shear peeling strength test [15].

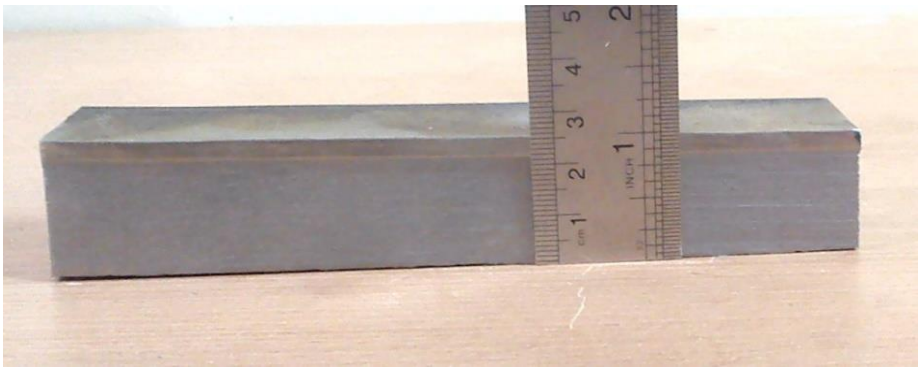

Fig. 2: Roll-bonded Clad plate specimen.

Table 1: SA 516 GR70 properties.

Yield stress (MPa)	**Ultimate Tensile Stress (MPa)**	**Elongation (%)**
387.96	520.79	**36**

Table 2: SS 316L properties.

$R_P0.2$ (MPa)	**$R_P1.0$ (MPa)**	**R_m (MPa)**	**A5 %**
303	351	605	**52**

To create a crack, a notch was first created by wire cut with a width of 0.2mm on one side of the sample and in the interface of the two layers. To ensure the crack nucleation, the specimen was subjected to flexural fatigue loading under 0.2 yielding stress with a frequency of 5 Hz for 60,000 cycles based on the ASTM E 1820 standard. Fig. 3 shows the grooves created by wire cut on the specimen.

To determine the critical strain energy (G_C) by measuring the area below the force-displacement diagram, a three-point bending loading test was performed by a Zwick device with a strain rate of 5mm/min. Fig. 4 shows the sample under loading.

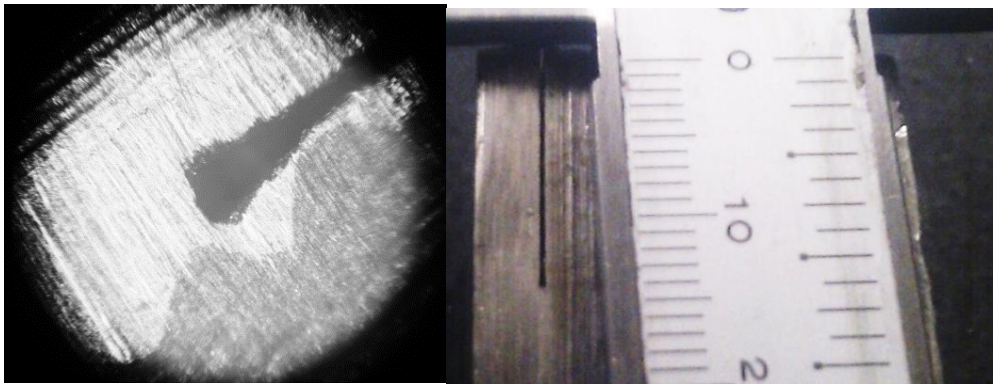

Fig. 2: The notch created in clad and base plate interface on the sample edge using wire cut, 50X optical microscope image

Simulation procedure

In this paper, ABAQUS software was used for the FEM investigation of the system. To this end, critical SERR was calculated by the virtual crack-closure technique (VCCT). This method was first proposed by Rybicki et al. [16] and developed by others [17], [18], [19], [20] . In this technique, the SERR value can be obtained by calculating the force and displacement of the nodes at the crack tip. For a two-dimensional model (Fig. 4a), the following equation can be expressed:

$$G_{\mathrm{I}} = \frac{1}{2b\Delta a} F_{Z1}(w_2 - w_3) \quad (4)$$

$$G_{\mathrm{II}} = \frac{1}{2b\Delta a} F_{X1}(u_2 - u_3) \quad (5)$$

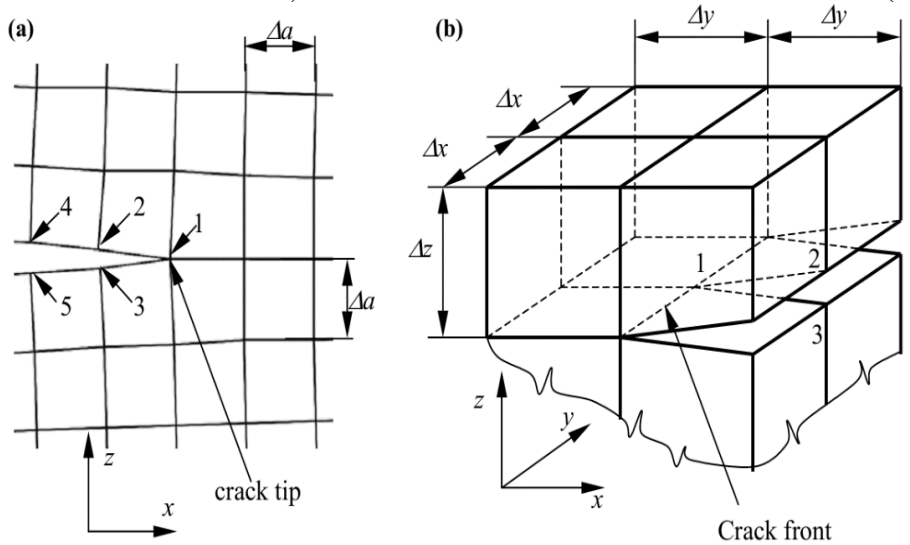

Fig. 3: Principles of VCCT.

In this regard, the applied force on the specific nodes in the crack growth path (marked in Fig. 4), as well as their displacement, was calculated. Each layer and its corresponding bonding area were separately modeled. The thickness of the bonding region was optimized by its ranging from zero (Full Model) to 1.5 mm (Tied Mesh).

In the TM model, the bonding region was modeled as a cohesive zone which retains its true thickness and is attached to the corresponding nodes of the surrounding layers by a movable constraint at both ends. This moving constraint preserves the equality of the degrees of freedom on both sides of the bond layer and eliminates the distance between adjacent layers thus, greatly reduces the complexity of bond region stresses.

The material assigned to the bonding layer in the TM mode was the traction separation and the delamination mechanism was assumed as quadratic. The maximum shear stress was assumed as the node separation-determining parameter which was obtained 382MPa according to the shear peeling test on the cladded plate (ISO 4587 standard).

The elements of the bonding layer were selected as cohesive elements, COH2D4, and their optimum size indicates the amount of crack growth, Δa, is one quarter the thickness of the bond area [21], [22]. Adjacent layer elements were linear with quadratic plane strain, CPE4I.

Material assigned to the bond layer was the traction separation with hardness coefficients of $K_{nn}=E_{11}/t$ and $K_{ns}=K_{ss}=G/t$ in which t is the thickness of the bonding layer, G shows the shear modulus (19.1GPa), and E_{11} and E_{22} denote Young's modulus along the x and y axes, respectively; which were equal to the average Young's modulus of adjacent layers. E_{33}=49.66GPa was calculated from $E=2G(1+\nu)$. The Poisson's ratio was assumed to be 0.3.

The two-step loading was static-general, taking into account the nonlinear deformation.

In the first step, the punch moves to the depth of the matrix and bends the plate, while in the second step, the punch penetrates the plate at a defined pressure. The punch was modeled as Analytical Rigid.

The force applied to the crack tip node (node 1 in Fig. 5) and the horizontal displacement of adjacent crack nodes (nodes 2 and 3 in Fig. 5) were taken as the output parameters. In order to calculate G at the starting point of crack growth by VCCT observing the first fall in the force-displacement diagram, the same values of force applied to node 1 and the horizontal displacement of nodes 2 and 3 were read. The value G was finally calculated by Eqs. 4 and 5. As the crack grew, the node 1 at the crack tip moved element by element. Fig. 6 shows the configuration and meshing of the model whereas Fig. 7 represents the stress distribution in the crack tip.

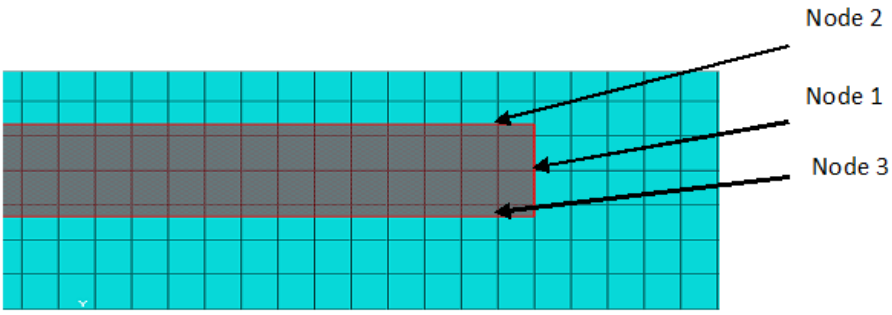

Figure 4: Meshing bonding and adjacent layers (TM with 1.5 mm thickness).

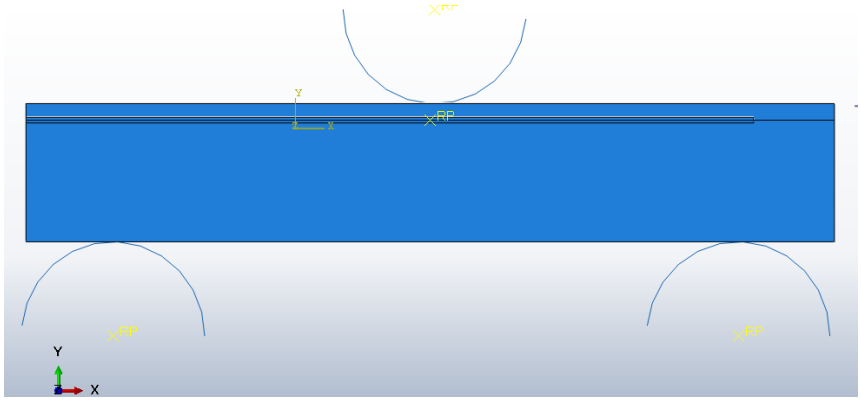

Figure 6: Configuration of the model.

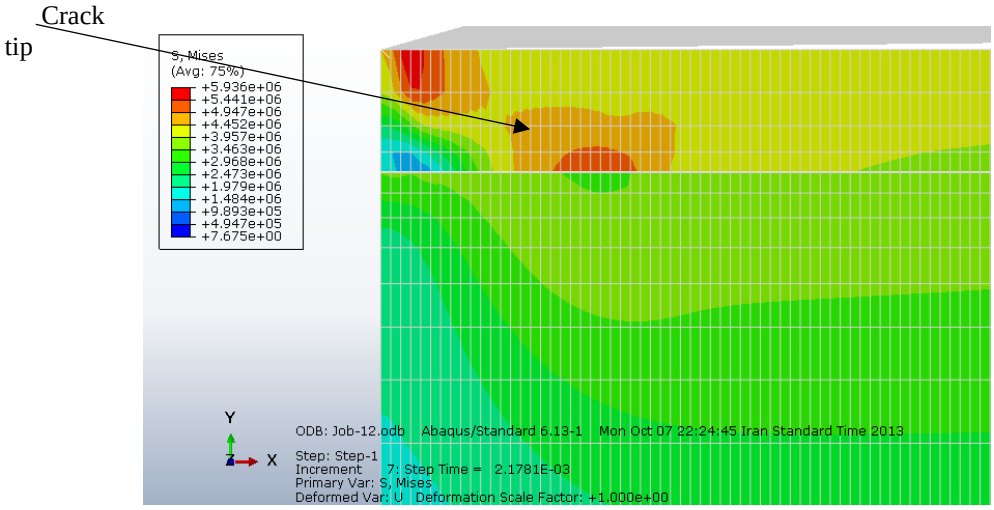

Figure 7: Stress distribution in the bonding area and crack tip (thickness of the bonding layer is 1mm).

Fig. 8 shows the force-displacement values. The G values obtained from the experimental and finite element methods are listed in Table 3 for different thicknesses. As shown, the FEM results significantly differed from the experimental results. In the model whose thickness of bonding area (or cohesive zone) was 0.25 mm, the Hour Glass phenomenon [23] occurred and the analysis did not reach the starting point of crack growth due to the excessive shrinkage of the elements and their high deformation. In the model with a cohesive zone thickness of 0.5 mm, the same thing happened but at a higher point. In the model with bond region thickness of 1.5mm, the width of the bonding element was larger than the size of the adjacent layer elements. Due to their high deformation, the analysis remained incomplete. Therefore, only the full method (FM) with zero bond thickness and the tied mesh method (TM) models with the bond thicknesses of 0.75, 1 and 1.25 mm were analyzed. The best fit to the experimental results was obtained at the thickness of 2 mm for the bonding elements.

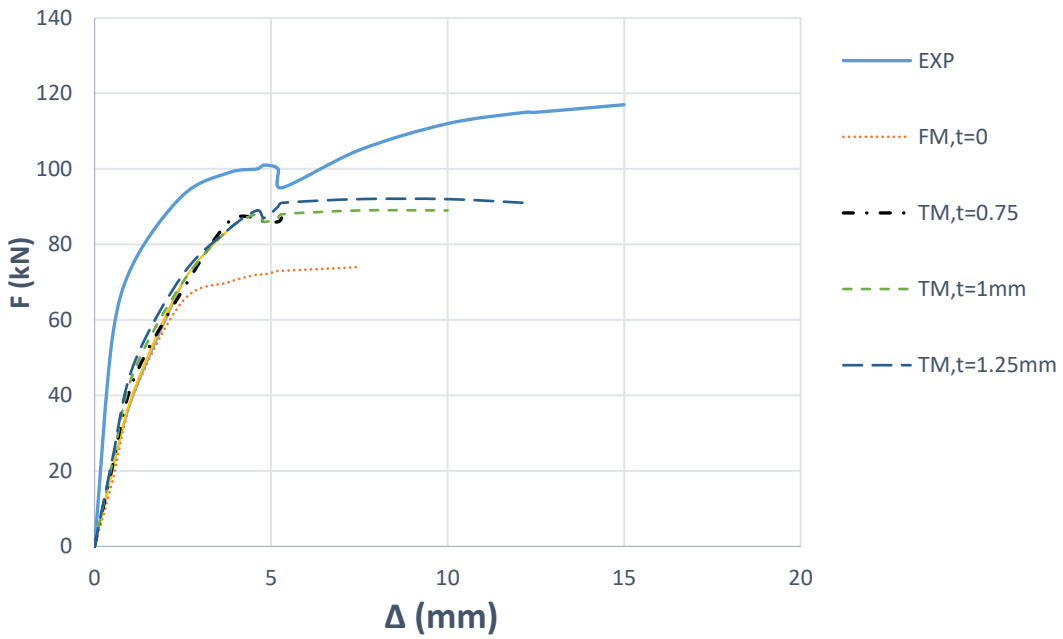

Figure 8: Numerical and experimental results.

Table 3: Comparison of G values needed to grow interlayer crack (G_{cr}) from the experimental test, Analytical solution (Ouyang and Li Eq. 3) and finite element model For different thicknesses of the bonding region (t).

	The area under the curve	Ouyang and Li	t=0	t=0.75	t=1	t=1.25

G_{cr}(J/mm)	12.42	12.12	7.623	10.297	10.521	10.482
Error value (%)	-	0.9	38.6	17.12	15.29	15.6

According to Fig. 8, the force-displacement diagram at the breakpoint showed a sudden drop followed by a hardening behavior. By viewing the microscopic image of the specimen and comparing it with the crack image before bending test, this behavior of the graph can be explained by the fact that in the force drop region, some cracks grew in the intermediate region of the two sheets as the force required by the crack growth in the bonding region was lower than adjacent layers [2] [5]. After some growth in the intermediate zone, the crack entered the softer zone (the laminate layer) and exhibited hard work behavior.

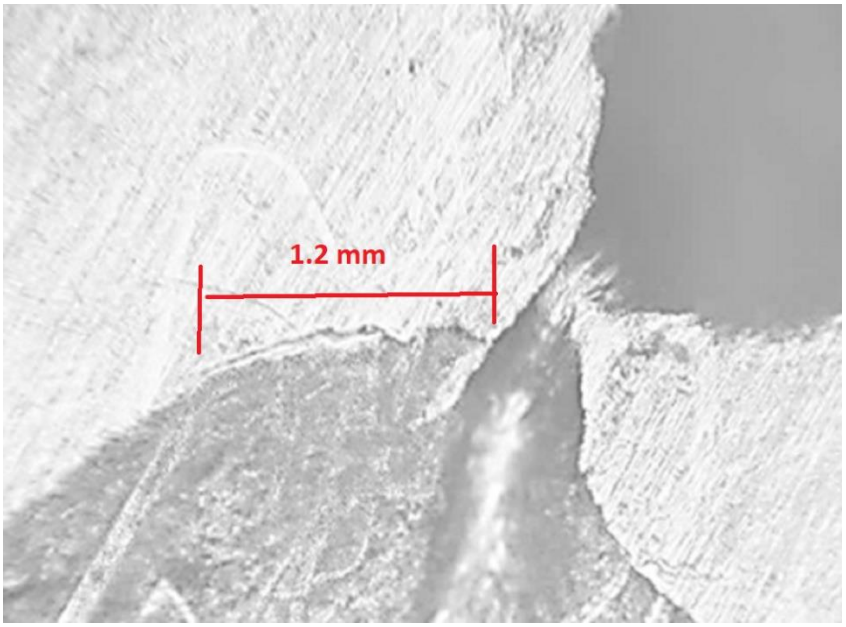

Figure 9: Crack grow after loading.

Design of Experiment

In this paper, the design of experiment (DOE) method as implemented in the surface response methodology (RSM) was used [24]**.** The following general form shows a response level for quadratic (and first) models.

$$y = \beta_0 + \sum_{i=1}^{k} \beta_i x_i + \sum_{i=1}^{k} \beta_{ii} x_i^2 + \sum_{i<j} \sum \beta_{ij} x_i x_j + \varepsilon$$

Design Expert 7.1.1 software was used to calculate the required matrices coefficients of β and draw the output charts. The studied parameters and their values are shown in Table 4.

Table 4: Maximum and minimum values of effective parameters on the delamination process.

Parameter	**Min**	**Max**
Pressing force (MPa)	14 (2000psi)	**35 (5000psi)**
Number of loading steps	3	**5**
Head radius (mm)	500	**4500**
Plate thickness (clad +base plate)	17+3	**57+3**
Friction coefficient	0.1	**0.3**
Shear peeling strength (MPa)	120	**280**

Results and Discussion

After performing the analysis and before estimating the mathematical function, it is necessary to examine the significance of the effect of control variables on the outputs. Table 5 shows the statistical summary of the data

analysis. By focusing on the regression-squared and predicted residual error sum of squares (PRESS), this table describes the status of the three linear models, the interaction effects (2F1), and the nonlinear quadratic model. Therefore, the quadratic model was proposed to estimate the effects of the parameters on the objective function due to its high regression coefficients and low squared error.

Table 5: Summary of Statistical Analysis of Existing Models.

Source	**Std. Dev.**	**R-Squared**	**PRESS**	
Linear	27.93	0.162	0.0299	
2F1	31.25	0.511	0.0543	
Quadratic	17.21	0.69	0.0214	**Suggested**

Table 6 shows the values of the design of experimental inputs and their corresponding results. Finally, the following equation was obtained to describe the effect of input parameters on the strain Energy Release Rate.

Table 6: Values of the experimental design input parameters and the obtained results

	A	**B**	**C**	**D**	**E**	**F**	**Result**
Run number	Force (MPa)	Radius (mm)	Thickness (mm)	Friction coefficient	Shear strength (MPa)	loading steps	**G_{II} (KJ/mm)**
1	35	4500	40	0.1	280	3	**0.0164**
2	14	4500	20	0.1	280	5	**0.0239**
3	35	500	60	0.3	280	3	**53.63**
4	14	4500	60	0.1	280	3	**2.8488**
5	35	500	60	0.3	280	5	**48.88**
6	24.5	4500	60	0.3	280	3	**3.017**
7	24.5	2500	20	0.2	200	3	**0.3835**
8	35	4500	60	0.3	200	3	**7.33**
9	24.5	500	20	0.3	120	5	**34.21**
10	35	500	60	0.1	280	5	**49.12**
11	14	2500	40	0.2	200	5	**1.591**
12	24.5	500	60	0.1	120	3	**19.476**
13	35	500	20	0.1	120	3	**40.49**
14	24.5	4500	60	0.3	280	5	**1.714**
15	14	500	20	0.3	280	4	**19.08**
16	14	2500	60	0.3	280	3	**0.153**
17	35	4500	20	0.3	120	3	**0.2511**
18	35	4500	20	0.3	280	5	**0.00302**
19	14	4500	20	0.2	280	3	**0.00106**
20	14	500	20	0.1	120	5	**33.61**

21	24.5	500	20	0.1	280	4	**17.42**
22	35	4500	20	0.3	120	5	**0.00375**
23	35	500	40	0.1	120	5	**29.1**
24	14	500	60	0.1	200	5	**38.81**
25	14	4500	20	0.3	200	4	**0.00308**
26	14	4500	60	0.1	120	5	**2.477**
27	29.75	2500	50	0.15	160	3	**13.583**
28	24.5	4500	20	0.1	120	3	**0.245**
29	35	500	20	0.3	200	5	**26.59**
30	35	4500	60	0.1	200	5	**2.209**
31	14	500	60	0.3	200	4	**49.64**
32	14	500	40	0.1	280	3	**13.88**
33	35	4500	20	0.1	200	5	**0.00127**
34	35	2500	60	0.3	120	3	**0.359**
35	14	4500	60	0.2	120	3	**1.367**
36	35	500	40	0.1	120	4	**14.02**
37	35	2500	60	0.3	120	5	**0.479**
38	24.5	500	60	0.3	120	3	**33.07**
39	14	4500	20	0.3	200	5	**0.000889**
40	35	500	20	0.3	200	3	**24.6**
41	14	500	20	0.3	280	5	**19.088**
42	35	500	20	0.2	280	5	**19.72**
43	14	500	20	0.3	120	3	**40.683**

$$G(J/mm) = -183.6 + 126.41 \times A - 1579.43 \times B + 373.85 \times C + 47.45 \times D - 57.20 \times E - 80.83 \times F$$
$$-1.37 \times AB + 101.48 \times AC - 52.81 \times AD + 300.13 \times AE - 223.06 \times AF - 315.78 \times BC$$
$$-175.14 \times BD + 160.11 \times BE - 28.73 \times BF + 77.6 \times CD + 581.31 \times CE + 99.95 \times CF$$
$$-84.09 \times DE - 2.57 \times DF - 74.51 \times EF + 441.38 \times A^2 + 1452.43 \times B^2$$
$$+830.41 \times C^2 - 763.30 \times D^2 + 9.14 \times E^2 + \varepsilon \quad (6)$$

In the above equation, A, B, C, D, E, and F are the pressing force, head radius, plate thickness, friction coefficient, shear strength in MP and number of press steps, respectively. Moreover, ε denotes the error or noise of the results. As shown in Eq. 6, the head radius had the greatest effect on G_{II}, followed by plate thickness, pressing force, number of pressing steps, shear strength of the sheet, and friction coefficient.

Figure 10 shows the effect of radius and thickness enhancement on the value of G. As can be seen, An increment in the head radius reduced the deformation in the intermediate region, thereby declining G. Increasing the thickness of the plate also raised the G value and consequently enhanced the probability of delamination. As the bond layer distance from the neutral axis of the plate increased, its corresponding deformation was raised by bending with a sharp increment in the stress of this area.

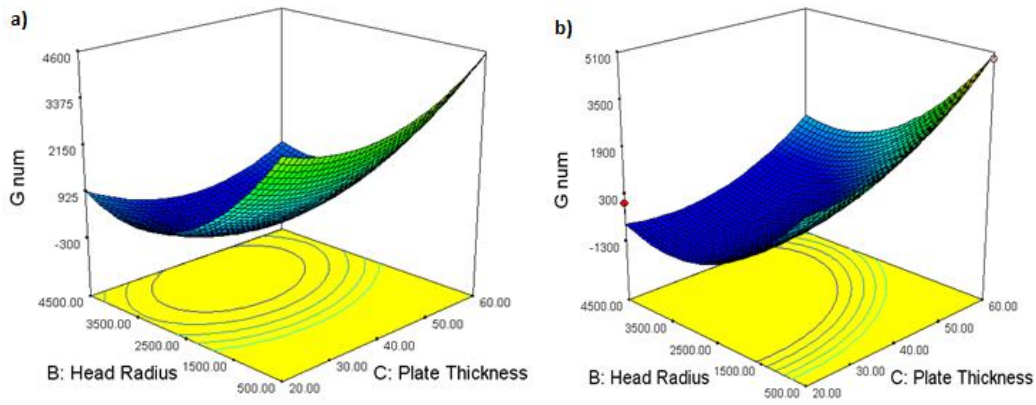

Fig. 10: Effect of radius and thickness increase on G when a) other parameters are minimum and b) other parameters are maximum.

The next influential parameter is the punch pressure, which increased by raising G. As can be seen in Fig. 11. If the punch pressure increased, the strain on the x-y plane of the bond plate increased as well, which raised the stress in this area. As result, the strain energy reached its critical value faster.

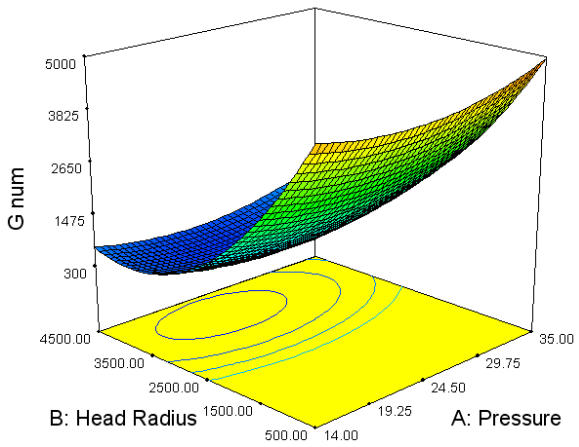

Fig. 11: Effect of punch pressure and head radius on G, Other Parameters are at the intermediate level.

Fig. 12 shows the effect of pressure on G for different shear strength values. For a high number of pressing steps (or low penetration depth), an increase in pressure decreased the G value at low shear strengths. This trend can be assigned to the increase in the pressure which prevented the sliding of the layers in the bonding area due to the friction phenomenon. According to Russell and Street [13], friction between crack surfaces absorbs some fracture energy. Gillespie et al. [25] obtained the amount of this energy reduction for the ENF sample through the finite element method. They concluded that the friction between the two cracks can absorb 2-4% of the fracture energy. An increase in the pressure enhanced the friction effect and thereby raised the amount of absorbed energy. This is particularly noticeable in high-thickness plates which require a large number of forming steps.

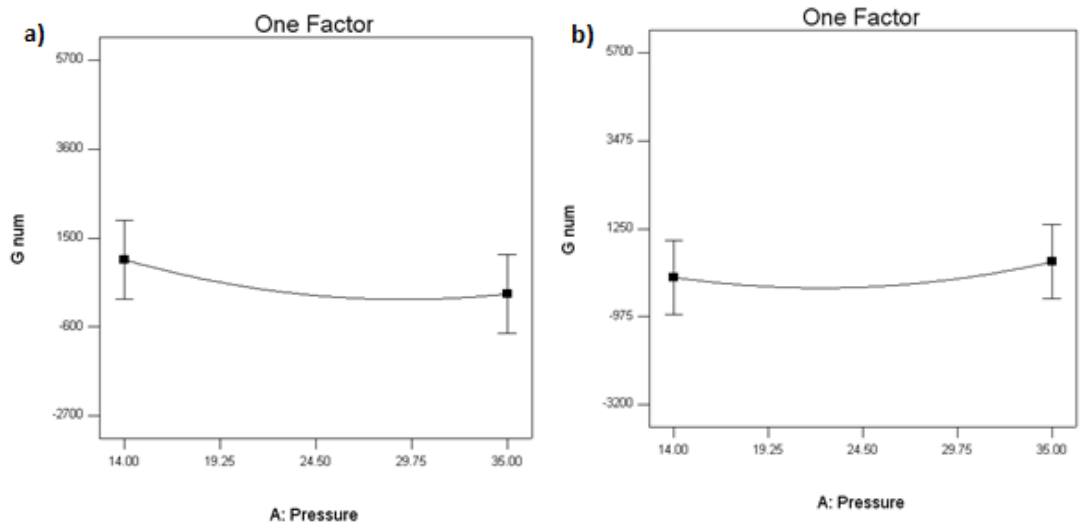

Figure 12: Effect of pressure on G value for the shear strength values of a) 120 Mpa and b) 280Mpa. The number of pressing steps was 5 and other parameters were at the intermediate level.

Fig. 13 shows the effect of thickness and radius on the delamination. For 5 forming steps, G values showed less dependence on the thickness and radius. The exact number of forming steps was determined when the critical value of the fracture energy, G_{IIC}, was obtained by testing the specimen. In the below figures, the blue area shows the safe area of formation.

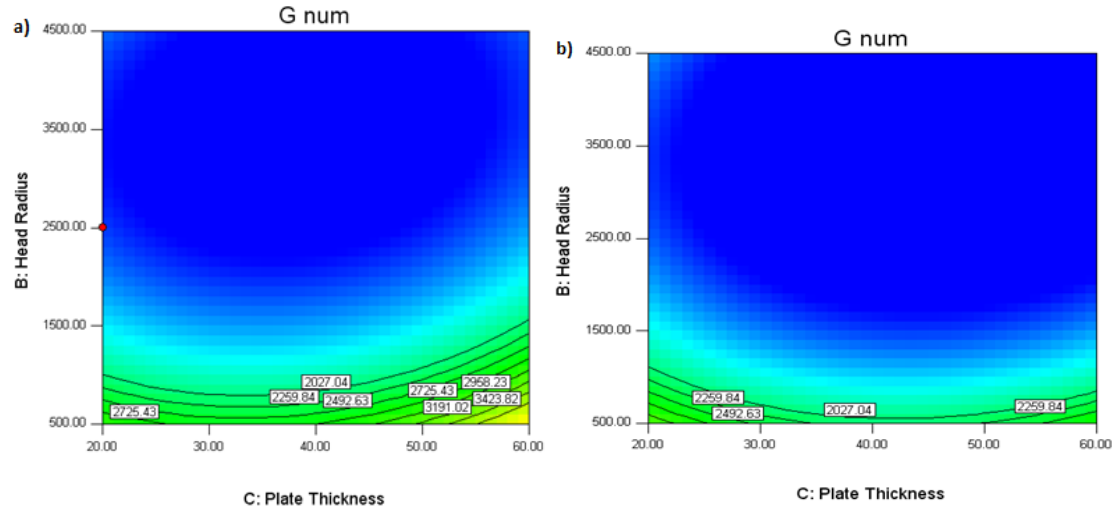

Fig. 13: Effect of thickness and radius on the delamination process for a) 3 and b) 5 pressing steps, other parameters were set at the intermediate level.

Fig. 14 shows the influence of plate thickness on the G value. According to Eq. 6, the interaction of thickness and shear strength has the greatest impact on the G value. As can be seen, for high penetration depth at each step (i.e. low number of steps) and low shear strength of the sheet, a rise in the sheet thickness decreased the G value. In this case (high thickness and low shear strength) changed the parameters to reduce the relative slip of adjacent layers at the bonding surface of the two sheets, hence decreasing the G value. Such a trend increased the pressure while declining the number of pressing steps.

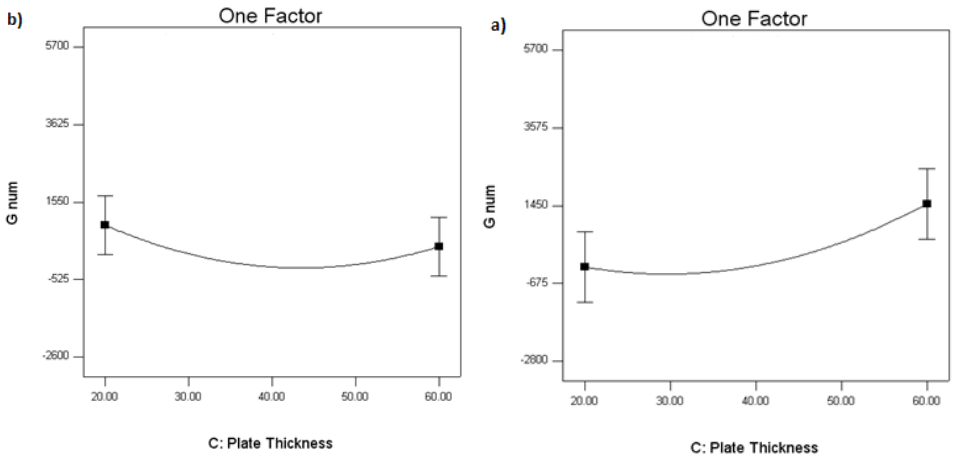

Fig. 14: Effect of thickness on G value for 3 pressing steps and a) Peeling shear strength of 280 Mpa and b) 120 Mpa.

Conclusion and some recommendations to avoid delamination

To determine the critical fracture toughness, a specimen was prepared from the plate its G_{IIC} value was measured by peeling shear test. Then by putting the effective parameters such as thickness, radius, and shear strength in Eq. 6, the G value was calculated and compared with the experimental G_{IIC} value. The following conclusions were made:

- If the calculated value is higher than the G_{IIC}, the plate may delaminate under these conditions. If the calculated value is very close to G_{IIC}, delamination can be prevented by changing the less effective parameters (e.g. decreasing the friction coefficient and increasing the number of pressing steps).
- For high plate thicknesses, variations in the shear strength of the sheet will not have a significant effect on the delamination. Thus, heat treatment to increase the bond strength prior to forming will be a waste of time and cost.
- According to the observations, for forming radii of 500mm or less, plates coated by explosive welding could also show interlayer detachment. Therefore, for radii below 500 mm, the base plate should be first formed and then the coating layer must be created by submerged arc welding with a strip electrode on the base metal. If necessary, the surface can be machined or ground.
- According to the results, for low shear strength, an increment in the pressing pressure will reduce the probability of interlayer separation. This is particularly noticeable in high-thickness plates that require a large number of forming steps. In these cases, the relative sliding of the layers should be avoided. For this purpose, the penetration depth and pressure of the forming can be increased.
- In the case of submerged arc welding or thermal spraying, if temperature rise is problematic and the plate cannot be coated in this way, a stress-relieving operation should be conducted between the forming steps.

References

1. A., G. A. (1921). The phenomena of rupture and flow in solids. *Philosophical Transactions of the Royal Society of London, Series A, Containing Papers of a Mathematical or Physical Character*, 163-198.
2. *Abaqus 6.8 documentation, part 3, Mesh module, Understanding adaptive remeshing.* (n.d.).
3. AndrásSzekrényes. (2012). Interlaminar stresses and energy release rates in delaminated orthotropic composite plates. *International Journal of Solids and Structures, 49*(18), 2460-2470.
4. AndrásSzekrényes, William MartinsVicente. (2012). Interlaminar fracture analysis in the GII–GIII plane using prestressed transparent composite beams. *Composites Part A: Applied Science and Manufacturing, 43*(1), 95-103.
5. ASTM A264. (n.d.).
6. B. X. Liu, Q.An, F. X. Yin, S. Wang, C. X. Chen. (2019). Interface formation and bonding mechanisms of hot-rolled stainless steel clad plate. *Journal of Materials Science, 54*(DOI: 10.1007/s10853-019-03581-x), 11357-11377.

7. Carreno F; Chao J; Pozuelo M; Ruano OA;. (2003). Microstructure and fracture properties of an ultrahigh carbon steel-mild steel laminated composite. *Scripta Mater, 1135*, 40-48.
8. E. F. Rybicki and M. F. Kanninen;. (1977). A Finite Element Calculation of Stress Intensity Factors by a Modified Crack Closure Integral. *Eng. Fracture Mech, 9*, 931-938.
9. E.Tschegg; H.O.K.Kirchner and M. Kocak. (1990). Cracks At The Ferrite-Austenite Interface. *Acta metall, mater, 3*, 469-487.
10. G Meneghetti, A Campagnolo, M Avalle, Davide Castagnetti, M Colussi, P Corigliano, Massimiliano De Agostinis, E Dragoni, V Fontanari, F Frendo, L Goglio, G Marannano, G Marulo, F Moroni, A Pantano, A Rebora, A Scattina, Andrea Spaggiari, B Zuccarello. (2018). Rapid evaluation of notch stress intensity factors using the peak stress method: Comparison of commercial finite element codes for a range of mesh patterns. *Fatigue & Fracture of Engineering Materials & Structures, 41*(5), 1044-1063.
11. G.E.P. Box, K.B. Wilson. (1951). On The Experimental Attainment of Optimum Conditions. *G.E.P. Box, K.B. Wilson, "On The Experimental Attainment of Optimum Conditions" J. of the Royal Statistical Society. Series B 13. P.1–45, 1951., Series B13*, 1-45.
12. Gillespie, J. W.; Carlsson, L. A.; Pipes, R. B.; Rothschilds R.; Trethewey; B. and Smiley A.;. (1985). *Delamination growth in composite materials final report.* NASA-CR-176416.
13. HengZhang, PizhongQiao. (2020). Virtual crack closure technique in peridynamic theory. *Computer Methods in Applied Mechanics and Engineering, 372*. doi:https://doi.org/10.1016/j.cma.2020.113318
14. Krueger, R. (2004). Virtual crack closure technique: History, approach, and applications. *Appl. Mech. Rev, 57*(2), 109-143. doi:https://doi.org/10.1115/1.1595677
15. Lee S.; Wadsworth J.; Sherby OD.;. (1991). Tensile properties of laminated composites based on ultrahigh carbon steel. *Compos Mater, 25*, 842-53.
16. LucaDi Stasio, ZoubirAyadib. (2019). Finite Element solution of the fiber/matrix interface crack problem: Convergence properties and mode mixity of the Virtual Crack Closure Technique. *Finite Elements in Analysis and Design, 167*. doi:https://doi.org/10.1016/j.finel.2019.103332
17. N.V.De Carvalho, G.E.Mabson, R.Krueger, L.R.Deobald. (2019). A new approach to model delamination growth in fatigue using the Virtual Crack Closure Technique without re-meshing. *Engineering Fracture Mechanics, 222*. doi:https://doi.org/10.1016/j.engfracmech.2019.106614
18. Nambu S.; Michiuchi M.; Inoue J.; Koseki T. (2009). Effect of interfacial bonding strength on tensile ductility of multilayered steel composites. *Composites Science and Technology, 69*, 1936–1941.
19. Pozuelo M; Carreno F; Caesi M; Ruano OA. (2007). Influence of interfaces on the mechanical properties of ultrahigh carbon steel multilayer laminates. *Int J, Mater Res, 98*, 47-52.
20. Russell A. J. & Street K. N. (1989). Moisture and temperature effects on the mixed-mode delamination fracture of unidirectional graphite/epoxy. Delamination and debonding of materials. *ASTM, STP*, 876.
21. Sung-Tae Hong K.; Scott Weil;. (2007). Niobium-clad 304L stainless steel PEMFC bipolar. *Journal of Power Sources, 168*, 408-41.
22. T.L.Anderson. (2005). *Fracture Mechanics: Fundamentals And Application, Third Edition.* Taylor and Francis CRC press.
23. Wang J.; Qiao P. (2004). On the energy release rate and mode mix of delaminated shear deformable composite plates. *International Journal of Solids and Structures, 41*, 2757-2779.
24. Zhenyu Ouyang; Guoqiang Li;. (2009). Nonlinear interface shear fracture of end notched flexure specimens. *International Journal of Solids and Structures, 46*, 2659-2668.
25. ZoltánJuhász, AndrásSzekrényes. (2017). The effect of delamination on the critical buckling force of composite plates: Experiment and simulation. *Composite Structures, 168*, 456-464.